ADVANCED MATERIALS
www.advmat.de

Bioinspired Quasi-3D Multiplexed Anti-Counterfeit Imaging via Self-Assembled and Nanoimprinted Photonic Architectures

*Xintao Lai, Qun Ren, Florian Vogelbacher, Wei E. I. Sha, Xiaoyu Hou, Xi Yao, Yanlin Song, and Mingzhu Li**

Innovative multiplexing technologies based on nano-optics for anti-counterfeiting have been proposed as overt and covert technologies to secure products and make them difficult to counterfeit. However, most of these nano-optical anti-counterfeiting materials are metasurfaces and metamaterials with complex and expensive fabrication process, often resulting in materials that are not damage tolerant. Highly efficient anti-counterfeiting technologies with easy fabrication process are targeted for intuitive and effective authentication of banknotes, secure documents, and goods packing. Here, a simple strategy exploiting self-assembling and nanoimprinting technique to fabricate a composite lattice photonic crystal architecture featuring full spatial control of light, multiplexed full-pixel imaging, and multichannel cryptography combined with customized algorithms is reported. In particular, the real-time encryption/recognition of mobile quick response codes and anti-counterfeiting labels on a postage stamp, encoded by the proposed photonic architecture, are both demonstrated. The wave optics of scattering, diffraction, and polarization process involved are also described, validated with numerical simulations and experiments. By introducing a new degree of freedom in the 3D space, the multichannel image switching exhibits unprecedented variability of encryption, providing a promising roadmap to achieve larger information capacity, better security, and higher definition for the benefit of modern anti-counterfeiting security.

1. Introduction

Counterfeit products, including forged banknotes, artworks, brands, and individual documents, are becoming an ever-growing global issue.[1,2] To achieve reliable security of information and reduce economic loss threatened by counterfeit goods, various novel information encryption strategies that can offer multiple optical states to convey distinct information have been proposed.[3–8] Among these strategies, optical multiplexing technology, which realizes multiple-image storage on a single material, has provided a new solution for improving the storage density of information, and demonstrates great advantages of design and prospects in applications. [9–11] Multiplexing technology combining several signals into one signal has been widely used in telecommunication networks. For the optical information encryption platform, multiplexing technology exploits the spatial distributions of light (e.g., amplitude, phase, and polarization) as different information channels

X. Lai, F. Vogelbacher, X. Hou, Y. Song, M. Li
Key Laboratory of Green Printing
Institute of Chemistry
Chinese Academy of Sciences
Beijing National Laboratory for Molecular Sciences
Beijing 100191, China
E-mail: mingzhu@iccas.ac.cn

X. Lai, X. Hou, Y. Song, M. Li
School of Chemistry and Chemical Engineering
University of Chinese Academy of Sciences
Beijing 100049, China

Q. Ren
School of Electrical and Information Engineering
Tianjin University
Tianjin 300072, China

W. E. I. Sha
Key Laboratory of Micro-nano Electronic Devices and Smart Systems of Zhejiang Province
College of Information Science and Electronic Engineering
Zhejiang University
Hangzhou 310027, China

X. Yao
Department of Biomedical Sciences
Department of Chemistry
City University of Hong Kong
Hong Kong, China

M. Li
Key Laboratory of Materials Processing and Mold
Zhengzhou University
Ministry of Education
Zhengzhou 450002, China

The ORCID identification number(s) for the author(s) of this article can be found under https://doi.org/10.1002/adma.202107243.

DOI: 10.1002/adma.202107243

to record, process, and store data. Thus, the use of optical multiplexing technology increases the difficulty of decryption by requiring would-be counterfeiters to take numerous measures to obtain concealed data and choose between different information.

The most common optical multiplexing technology is based on costly metasurfaces/metamaterials with extraordinary capabilities of light manipulation, where different holographic images are encoded along multiple optical dimensions.[12–17] However, as these metasurfaces represent 2D spatial modulation, the strength of light-matter interactions is constrained by the short optical path lengths, resulting in low image quality; the functionalities including intrinsic chirality and polarization rotation (which are properties of 3D objects) are inaccessible by the 2D layer. Therefore, these candidates are incapable of encrypting information in the third dimension. This ability could allow for high-density information storage and enable advanced encryption. Although the bulk metamaterials can achieve 3D modulation and encryption, they are hindered by complex and expensive fabrication processes (such as lithography, chemical vapor deposition, and others) as well as mechanical damage through cracking.[18,19] For wavelength-controlled image switching, the cross-talk among different wavelengths remains a challenge.

Photonic crystals (PCs) are artificial periodic structures with a photonic band gap that have strong modulation of light propagation, showing great application potential for the development of anti-counterfeiting technology.[3,5] In particular, self-assembled colloidal PCs and their derivatives have been widely used due to their simple fabrication, low cost, and scalability. In responsive colloidal PCs, structural color materials are integrated with functional responsive materials (e.g., thermoresponse, biological response, vapor response, and/or photoresponse), providing a valid strategy for information multiplexing.[20–33] For example, Zhang et al. reported a bilayer PC which realized multichannel image switching relying on the different response of the two layers.[31] Some studies combined PC with fluorescent molecular components to increase the number of optical channels of multichannel PC encryptions.[22,23,30] Unfortunately, challenges remain with these multichannel PC materials: i) the finite fatigue life of the responsive components may cause material failure, which will hamper their durability and eventually lead to information loss; and ii) they only have single-plane imaging and the security is insufficient.

The hierarchical structure of biomaterials found in nature that generate exceptional optics has been the subject of intense research. Varieties of wonderful optical effects, such as color mixing, polarization, ultra-whiteness, dynamic structural color, and many others, occur from these structures.[34] In this study, we developed a new technique for advanced multidimensional crypto-information applications, inspired by the wings of the *Papilio palinurus* butterfly. The wings of this butterfly exhibit polarization-related colors produced by the hierarchical structure of periodic micro- and nanostructures (**Figure 1**a,b). Under oblique light, the butterfly wings have visibly vivid green color due to the periodic nanostructure (Figure 1b, inset) while the green zone of the wing turns black observed with a polarizer (α) rotated from 0° to 90°. It has been demonstrated that the polarization effect originates from multiple reflections of the incident light in the concavities of the *P. palinurus* wings.[35,36]

Herein, inspired by the polarization effect of *P. palinurus*, we propose a quasi-3D photonic architecture of a polarization-sensitive photonic crystal composite film (PCCF) through self-assembling and nanoimprinting technique. The prepared PCCF features full spatial control of light, multiplexed full-pixel imaging, and multichannel cryptography simultaneously. The composite lattice photonic crystal structure of PCCF consists of a 2D PC of a closely packed monolayer of polystyrene (PS) spheres ($d_{PS} \approx 600$ nm) containing a periodic array of micro-shallow pits ($P \approx 2.5$ μm, $H \approx 120$ nm), as shown in Figure S1 (Supporting Information). Taking advantage of the composite lattice structure of a PCCF, multichannel image switching can be realized as the scattering and s/p-polarized diffraction processes occur in this proposed quasi-3D photonic architecture. The PCCF is iridescent at characteristic angles when observed from either the same side or the opposite side of the incident light. In addition, the light diffracted by the PCCF is polarized (Figure 1e). It is demonstrated that the PCCF can provide a variety of encryption ways for encoding patterns and switching multi-images through combining with customizable cryptography algorithms. To prove this concept, we fabricated real-time encryption/recognition mobile quick response (QR) codes and anti-counterfeiting labels on a postage stamp by encoding them with the proposed photonic architecture. Simultaneously, the proposed PCCF to control the light field in 3D space, exploiting a facile, high-efficiency, precise fabrication process, is of great significance to increase the capacity of information storage and the dimension of the encryption. Overall, a composite lattice PC architecture, composed of multiple lattice periodicities of conventional PCs, provides an exciting new route for information multiplexing by offering a new degree of freedom to control light in 3D space. This strategy opens a covert 3D way for high-density information storage and advanced encryption, which is able to protect private information from unauthorized access, fracture, or destruction.

2. Results and Discussion

2.1. Fabrication of Quasi-3D Photonic Architectures

Figure 1c illustrates the PCCF fabrication method combining self-assembling and nanoimprinting technique. First, a 2D PC was fabricated using an air-water interface self-assembly method (details can be found in the Supporting Information).[37,38] Next, an orderly closely packed monolayer PCCF with a periodic array of micro-shallow pit structures was obtained by pressing a monolayer silica colloidal template (MSCT) stamp on the 2D PC. The MSCT was fabricated by an unidirectional rubbing method and a heat-treatment process (details can be found in the Supporting Information).[39] The silica spheres were modified with 1*H*,1*H*,2*H*,2*H*-perfluorooctyltrichlorosilane (PFOTS) and then thermally treated at 70 °C for 6 h. The prepared MSCT serves as a template for imprinting. Then, the predefined patterns were directly transferred through imprinting the MSCT onto the 2D PC films with a high pressure (1 bar, 1 min). This approach is simple, cost-efficient, and reproducible.

The fabricated composite structure exhibits multiple optical effects, including scattering, diffraction, and polarization, as

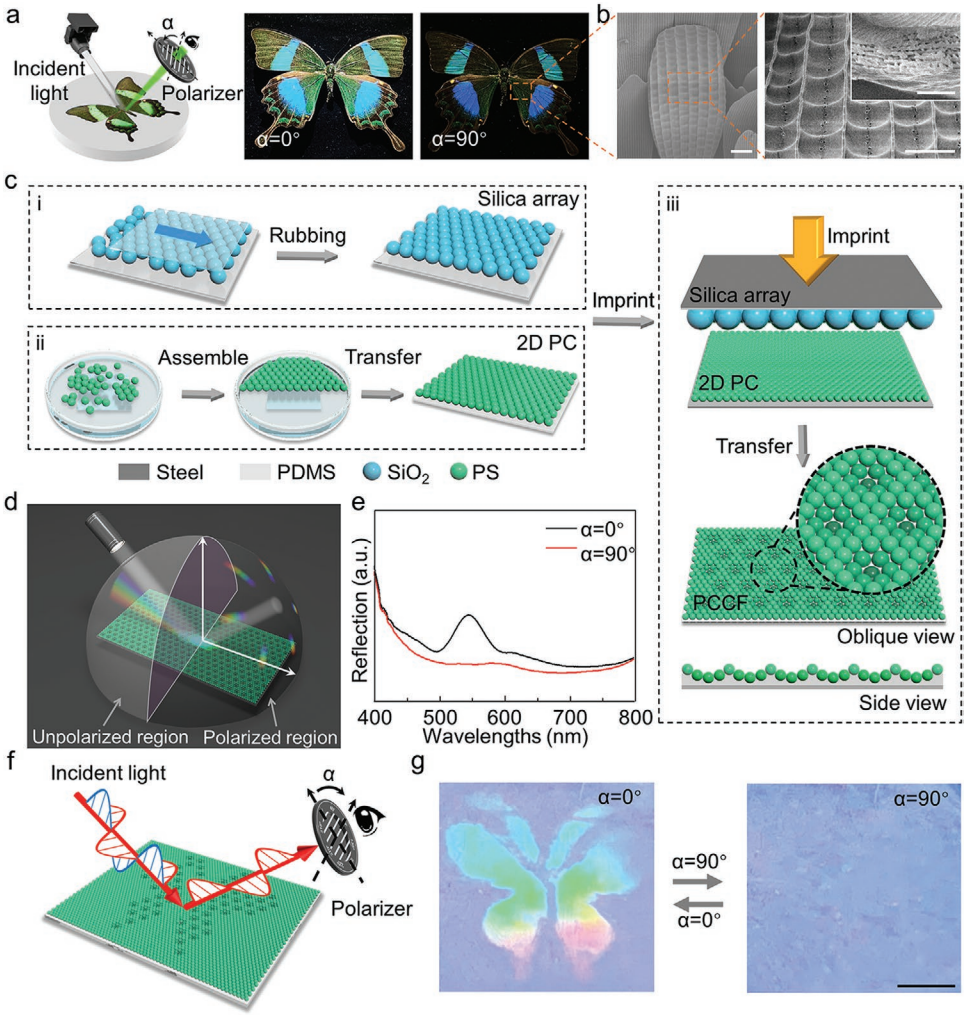

Figure 1. Design and the fundamentals of the photonic crystal composite film. a) Schematic of the experimental setup to characterize the structural color of *P. palinurus*. b) SEM images of the scales of *P. Palinurus* (inset: the cross-sectional view of the scales). Scale bars: 20 µm (*Left*), 10 µm (*Right*), and 1 µm (*Inset*). c) Schematic of the processes for the fabrication of i) the 2D PC, ii) MSCT, and iii) PCCF. The MSCT and 2D PC are pressed together by using a plier-like tool. Then a period array of micro-shallow pit structure is obtained. d) Schematic of the light propagation. e) The experimental polarization-dependent spectra of the diffraction of the PCCF. f) Schematics of the experimental setup to characterize the polarization of light reflected from a PCCF. g) Optical images of the patterned PCCF under the polarizer. The PCCF-structured butterfly disappears while the polarizer is rotated from 0° to 90°. Scale bar: 5 mm.

shown in Figure 1d,e. The schematic presents the different color response of the PCCF for unpolarized white light at 45° incidence: i) a full-color variation as the view angle changes when observed from the incident light side; ii) a set of multi-chromatic color patches, which are aligned in a hexagonal structure, appears at the opposite side of the incident light, showing color variation from purple to red with increasing distance from the reflection beam; and iii) the diffraction beams and reflection beam are both polarized light in the zone against the incident irradiation (Figure 1e; Figure S2, Supporting Information).

Furthermore, we fabricated a PCCF with a butterfly pattern to demonstrate the polarization properties more intuitively. Figure 1f shows the schematic of the experimental setup to characterize the polarized light reflected from the PCCF via rotating the polarizer. In the typical experiment, the PCCF-structured butterfly exhibits bright color under the reflection view angle of 25° (observed from the opposite side of the incident light), as shown in Figure 1g, *Left*. In contrast, the PCCF-structured butterfly disappears while the position of the polarizer is rotated from 0° to 90° (Figure 1g, *Right*). Meanwhile, the experimental polarization-related reflectance spectrum shows that the intensity of the reflected light is nearly extinguished at $\alpha = 90°$ (Figure 1e), which corresponds well with the imaging results. These results demonstrate that the PCCF possesses excellent polarization properties.

2.2. Characterization of Microstructure and Optical Properties of the PCCF

Figure 2a and Figures S3 and S4 (Supporting Information) demonstrate the monolayer ordered microstructure of the 2D

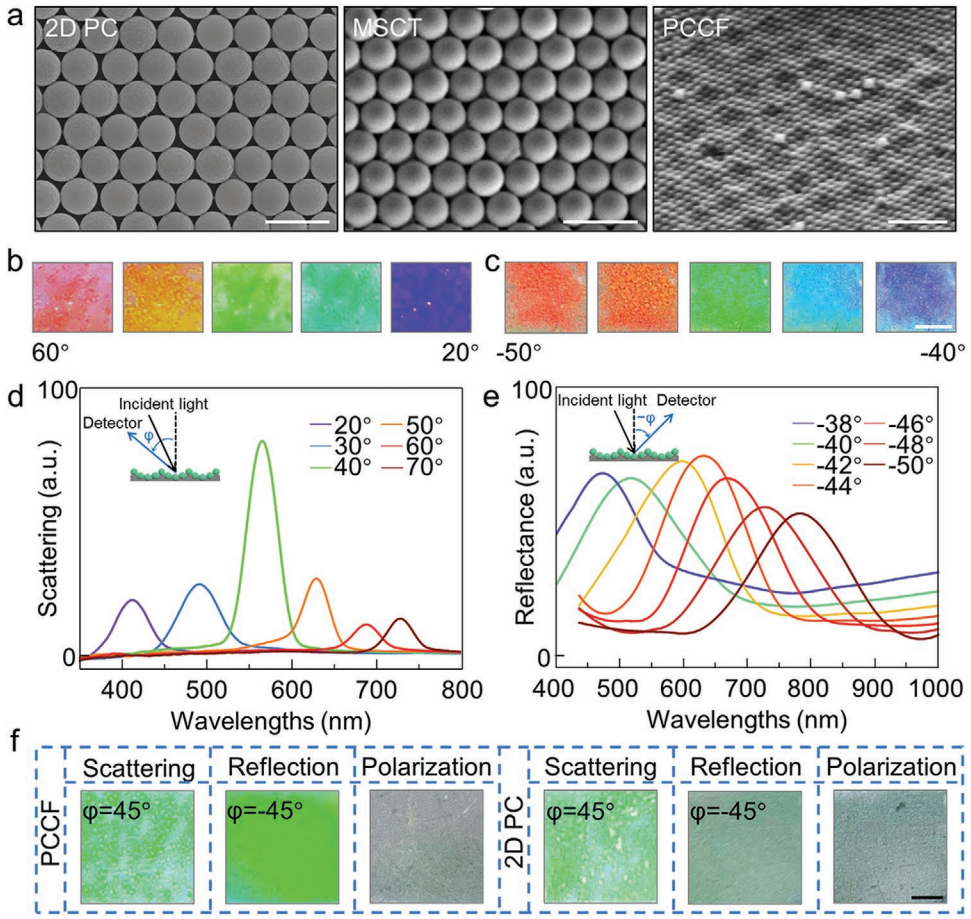

Figure 2. Morphological and optical characterization. a) SEM images of 2D PC, MSCT, and PCCF, respectively. Scale bars: 1 µm (*Left*), 5 µm (*Center*), and 5 µm (*Right*). b, c) Optical images of the PCCF at different viewing angles. Scale bar: 2 mm. d) Scattering spectra under ≈25° incident of the PCCFs. e) Reflectance spectra under ≈25° incident of the PCCF. f) Optical images of the 2D PC and PCCF at different viewing modes. Scale bar: 3 mm.

PC, MSCT, and PCCF, respectively. The results clearly indicate that self-assembled monolayer microspheres are closely packed with each other and arranged in a 2D hexagonal lattice.

Subsequently, an atomic force microscope (AFM) was employed to characterize the corresponding depth profiles of the PCCF sample, as shown in Figure S5 (Supporting Information). An orderly, closely packed, long-range ordered monolayer PCCF with a regular micro-shallow pit structure is clearly shown (Figure S5a,b, Supporting Information). The PCCF has a bilayer structure with 2D periods of 600 nm and 2.5 µm, respectively. The results match the corresponding scanning electron microscope (SEM) images (Figure 2a). Moreover, the height profile scanned across the PCCF shows that the degree of the deformation of the micro-shallow pit structure is about 120 nm and does not fluctuate much (Figure S5c, Supporting Information). Hence, we successfully verified that there are micro-shallow pit structures upon the PCCF, and the variation of concavity height gives rise to a color appearance and the polarization effect, showing distinctly different optical features compared with the 2D PC.

Next, we characterized the optical properties of the PCCF, as shown in Figure 2b–e. To systematically quantify the light scattering, diffraction, and polarization of the PCCF, we projected these light beams onto a translucent hemispherical screen and made a multi-directional observation, as shown in Figure S6 (Supporting Information). To clearly display the structural color variation of the PCCF at different viewing angles, we used a digital camera to take photos of the samples at different viewing angles, as shown in Figure 2b,c. When observed from the incident light side, the color gradually turns from purple to pink with the increasing viewing angle from ≈20° to ≈60°. When observing from the reflected light side, the color gradually turns from purple to red with the increasing viewing angle from ≈-40° to ≈-50°. In addition, the colors of the digital photos are basically consistent with the coordinates in the International Commission on Illumination (CIE) chromaticity diagram (Figure S7, Supporting Information) obtained by the scattering and reflection spectrum of the PCCF in Figure 2d,e. According to the scattering spectrum, the PCCF exhibits red-shifted diffraction peaks from ≈487 to ≈708 nm under different viewing angles from ≈20° to ≈60° (Figure 2b), which is consistent with the scattering spectrum of the 2D PC (Figure S8, Supporting Information). Furthermore, the reflection spectrum is similar to the MSCT, which shows broad diffraction peaks that red-shifted from ≈481 to ≈796 nm under different viewing angles from ≈-40° to ≈-50° (Figure 2e; Figure S9, Supporting

Information). Moreover, we compared the different color responses of the 2D PC and the PCCF. As a result, there are no more hexagonal polarized-related diffraction beams for the 2D PC, as shown in Figure 2f and Figure S8 (Supporting Information). Hence, these results prove that the PCCF was prepared by the imprint method to achieve the superposition of structural colors.

2.3. Numerical Simulations of Scattering, Diffraction, and Polarization

According to Bragg's law, these 2D hexagonal arrays diffract light at different angles depending upon the wavelength of the incident light.[40,41] The 2D diffraction condition is

$$n_i \sin\theta_1 + n_j \sin\theta_2 = M\frac{\lambda}{D} \tag{1}$$

where θ_1 is the angle of incidence, θ_2 is the diffraction angle, M is the diffraction order, λ is the diffraction wavelength, D is the lattice distance, and, n_i and n_j are the refractive indices of the incident and diffraction media ($n_i = n_j = 1$), respectively. For the case where θ_1 and λ are fixed, the diffraction angle is determined by the lattice constant D, such that the diffraction angle could be written as

$$\theta_2 = \sin^{-1}\left(M\frac{\lambda}{D} - \sin\theta_1\right) \tag{2}$$

In this experiment, the incoming light beam (monochromatic light, λ = 650 nm) was perpendicular to the samples, and a digital camera was used to record the diffraction patterns of the screen. The experimental setup is sketched in Figure S10a (Supporting Information). Since $\theta_1 = 0$, then Equation (2) is simplified to

$$\theta_2 = \sin^{-1}\left(M\frac{\lambda}{D}\right) \tag{3}$$

It can be inferred that to form a diffraction pattern, θ_2 needs to be real, thus we need

$$-1 < M\frac{\lambda}{D} < 1 \tag{4}$$

where M is an integer, $D = \sqrt{3}d/2$, d is the nearest neighbor particle spacing. Figure S10b (Supporting Information) shows the calculated first-order far-field diffraction patterns for transmission arising from a plane wave at normal incidence at a wavelength of 650 nm. At this wavelength, the 2D PC (d = 600 nm) does not satisfy in Equation (4) and only the transmitted beam is visible, as shown in Figure S10b, *Left* (Supporting Information). In contrast, both the MSCT and PCCF structure support the first-order diffraction, and the characteristic diffraction pattern of a hexagonal lattice is visible. For the MSCT (d = 2.5 μm), there are two values of M that satisfy the in Equation (4), thus we can see the first-order diffraction pattern (Figure S10b, *Center*, Supporting Information). As for the PCCF, the bilayer film is composed of two kinds of 2D structures with different lattice constants and closely packed with high periodicity, as shown in Figure S10b, *Right* (Supporting Information). Hence, the characteristic diffraction pattern of a hexagonal lattice is visible (Figure S10b, *Right*, Supporting Information). Actually, it can be inferred from in Equation (4) that the diffraction pattern will appear only when the lattice constant D is larger than λ. This means that at a wavelength of 650 nm, the diffraction spots disappear from the screen for lattice constants below 650 nm. Additionally, the experimental findings are in good agreement with the simulation results, as shown in Figure S10c (Supporting Information). Next, we measured the diffractive patterns by using a back-scattering optical setup (Figure S10d, Supporting Information) to study the intrinsic optical characteristics of these samples, and the results are similar (Figure S10e, Supporting Information).

The hexagonal gratings characterized by PCCF can be essentially represented as a combination of three sets of 1D gratings with the same spacing. As illustrated in **Figure 3**a, grating group 2 (indicated by black dotted lines) and 3 (yellow solid lines) are rotated by 60° and 120° relative to grating group 1 (blue dashed lines), respectively. The diffraction orders of bright fringes are indexed in the 2D diffraction pattern as shown in Figure 3b. The disappearance of diffraction orders such as (0, ±1) is attributed to the superposition between the maximum interference and minimum diffraction of hexagonal gratings. Taking alone the case of 1D grating as present in Figure 3c–e, the diffraction intensity is determined by the formula [42]

$$I = A_0^2\left(\frac{\sin\alpha}{\alpha}\right)^2\left(\frac{\sin N\beta}{\sin\beta}\right)^2 \tag{5}$$

where $\alpha = \frac{\pi q}{\lambda}\sin\theta_i$, $\beta = \frac{\pi P}{\lambda}\sin\theta$, A_0 is the diffraction amplitude at 0° incident angle, q is the length of the reflecting region (as labeled in Figure 3d), P is the grating constant, θ_i is the incident angle, θ is the diffraction angle, and N is the number of grating units. Inferring from Equation (5), the diffraction phenomenon of grating is a combined effect between the interference of reflection and the diffraction of a grating unit (PS sphere), which depends on the reflection length q and grating constant P. The position of the first dark fringe (first principle minimum), which determines the radius of the principal maximum diffraction, can be obtained from the Fraunhofer diffraction equation $P\sin\theta = (M+1)\lambda$, ($M$ = 0), hence

$$\beta = \frac{\pi P}{\lambda}\sin\theta = \pi \tag{6}$$

Equation (6) reveals the inversion relationship between the grating constant and diffraction angle, which decides the scope of light spot in the center. Via the imprinting procedure, the PCCF presents as an echelon grating with shorter grating constant P_3 (compared with P_2 of the stamp in Figure 3c) (Figure 3e), which increases the diffraction angle and thus extends the bright spot region in the center. The enhancement of the principal maximum diffraction is at the expense of weakening the intensity of the secondary maximum diffraction, which makes each hollow in the PCCF to be a pixel of the

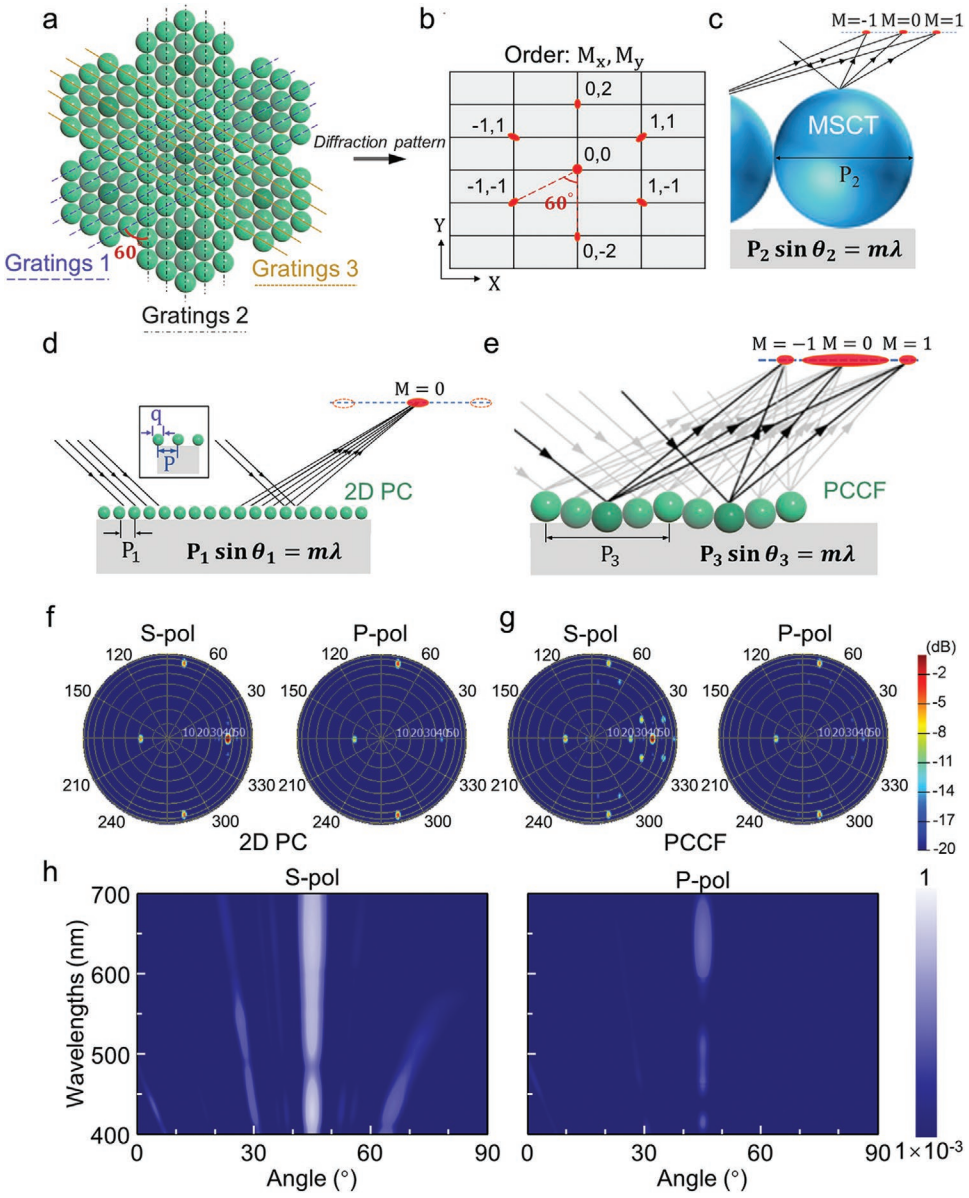

Figure 3. Underlying physics and numerical simulations of PCCF. a) Top view of the configuration of PCCF. b) Indexation of diffraction order in the diffraction pattern of hexagonal gratings. c-e) Schematics of the diffraction effect in MSCT, 2D PC, and imprinted gratings, respectively. f, g) Numerically calculated polarization-dependent far-field patterns of PCCF and 2D PC at a wavelength of 532 nm. h) Dispersion of the output beams obtained by numerical calculations.

imaging for high definition. In the case of 2D PC, as presented in Figure 3d, the period corresponding to a 1D grating is much less than for the MSCT and PCCF (Figure 3c,e), so that the zero-order diffraction dominates in the diffraction pattern, whereas other diffraction orders disappear. This physical reasoning is also verified in the simulation and experiment result as shown in the first column of Figure S10b,c (Supporting Information).

To further reveal the optical characteristics of the PCCF, we did numerical simulations of the scattering effect of a 2D PC and PCCF structure at a wavelength of 532 nm employing the finite-difference time-domain method, as shown in Figure 3f–h. The far-field numerical calculations of the 2D PC for a plane wave incident at 45° with respect to the normal of the sample surface show the characteristic pattern from the periodic hexagonal surface, i.e., a strong reflection at an output angle which equals the input angle, and the first-order diffractions. Because of the short lattice constant and the 45° input angle, only three out of the six first-order diffractions are visible. For the PCCF, the combination of two hexagonal lattices with different lattice constants results in a diffraction pattern similar to the 2D PC with an extra superimposed small angle hexagonal pattern for each diffracted beam, which is visible in the far-field plots in Figure 3g, and is in agreement with the theoretical assessment above. The simulations reveal a strong polarization dependence of the reflection and diffraction intensities. For the s-polarization, the far-field pattern is stronger than that from the p-polarization. The

angle-resolved spectral characteristics of PCCF for both polarizations are shown in Figure 3h. The reflected light at 45° is independent of wavelength. In contrast, the diffracted beams exhibit a wavelength dependence, which results in vibrant structural colors. Additionally, the reflection and diffraction patterns show characteristic spectral fingerprints related to the PC modes. For the p-polarized input, the reflection and diffraction intensity are significantly lower than that from the s-polarization.

Furthermore, the mechanism of the polarized-related structural color of PCCF has also been clarified. Visible light is an electromagnetic wave that consists of an oscillating electric field and a magnetic field, which are perpendicular to each other. An important intrinsic characteristic of electromagnetic wave is polarization.[43] Polarized light refers to the light for which the oscillation direction of the light vector is unchanged or has some regular variations. In linear polarization, the light vector oscillation direction is only limited in a certain plane that cannot be completely distinguished by human eyes.[44] Generally, visible light (generated from the sun, flames, fluorescent lamps, or other sources) that can be seen as an equal mixture of linear polarization light is called unpolarized light.

Linearly polarized light can be produced by passing unpolarized light through a polarizer, which allows waves of only one polarization to pass through. In addition, there is one special angle of incidence at which the reflected light at a material boundary is completely polarized perpendicular with respect to the plane of incidence, which is called the Brewster's angle. Thus, the light will become completely polarized from a reflecting surface when it is incident to the surface at Brewster's angle having a tangent equal to the ratio of the two materials' refractive index. According to the well-known Fresnel's equations, the Brewster's angle can be described as follows

$$\theta_B = \arctan\left(n_2/n_1\right) \tag{7}$$

where n_1 and n_2 refer to the refractive index of air ($n_1 \approx 1$) and the reflecting material, respectively, and θ_B refers to the Brewster's angle. In our experiment, we use the effective refractive index n_{eff} of the PCCF to replace n_2 that can be calculated as follows

$$n_{\text{eff}} = \sqrt{n_1^2 V_1 + n_2^2 V_2} \tag{8}$$

where V_1 and V_2 refer to the air and PS volume fraction of the PCCF, respectively. As a result, the Brewster's angle of the PCCF calculated by Equation (7) and Equation (8) here is around 56°. In our experiments, the incident angle is very close to the Brewster's angle, which gives rise to the obvious polarization effect. Here, we can define a polarization contrast P_c as

$$P_c = \frac{R_s - R_p}{R_s + R_p} \tag{9}$$

The reflectance of s-polarization (R_s) and p-polarization (R_p) can be written as [43]

$$R_s = \frac{\sin^2(\theta_1 - \theta_2)}{\sin^2(\theta_1 + \theta_2)} \tag{10}$$

$$R_p = \frac{\tan^2(\theta_1 - \theta_2)}{\tan^2(\theta_1 + \theta_2)} \tag{11}$$

where θ_1 is the incident angle and θ_2 is the transmitted angle. As a result, the calculated polarization contrast is ≈0.86. The high polarization contrast of the PCCF means the diffraction from the periodic array of micro-shallow pits of the PCCF is nearly perfectly linearly polarized. Thus, polarized structural color occurs when the incident light is close to the Brewster's angle.

The proposed PCCF has extraordinary capabilities of encryption. Firstly, the cryptogram can be encoded into the multichannel image of the PCCF (i.e., the scattering channel and s/p-polarized diffraction channels) and then combined with encryption algorithms. For example, the PCCF shows different optical responses, and therefore the numbers "1", "2", and "3" can be assigned to these channels to produce a cryptogram, as shown in the keytab in Table 1 (Supporting Information). According to the permutation and combination rule, there are several combinations of the numbers to form the cryptogram (Table 2, Supporting Information). Thus, the usage of the encryption algorithm will improve the security of this coding strategy. Secondly, the polarizer is an indispensable part of the decryption process. In the absence of a polarizer, the attacker can get only wrong information. Finally, several cryptograms based on the scattering channel and s/p-polarized diffraction channels could be generated through this kind of algorithm encryption, and only the right combination of channels could receive the correct cryptogram. It would make the codes more uncertain and harder to decipher so as to increase the security and achieve anti-counterfeiting.

2.4. Practical Demonstrations of Encryption

Recently, QR codes have become the most widely used coded system in the world because of their remarkable advantages (e.g., large storage capacity, high error-correction capability, and low cost), and they have been applied in various fields, including manufacturing, commercial activities, health care, and so on. However, it is undesirable to publicize the QR codes in some situations. Our proposed structural material can provide a cryptographic functionality to QR codes in this case. As shown in **Figure 4**a, we constructed an encoding layer of PCCF onto the QR code (2.5 cm × 2.5 cm) to verify the applicability of the polarization-sensitive material. Then, a commercially available smartphone with QR code scanning function was used to identify the QR code signal. Figure 4b–d demonstrates the schematic of the processes of the QR code authentication. Specifically, the top layer exhibited bright green structural color that concealed the bottom layer when observed from the incident light side. Thus, the QR code could not be decrypted by the smartphone, as shown in Figure 4b. In addition, the top layer showed an iridescent "butterfly" pattern that sheltered the bottom layer when viewed from the opposite side of the incident light, which resulted in the false image (Figure 4c). In contrast, the bottom QR code could be read out by the smartphone through rotating the polarizer to a specific polarization angle (i.e., $\alpha = 90°$), as shown in Figure 4d and Movie S1 (Supporting

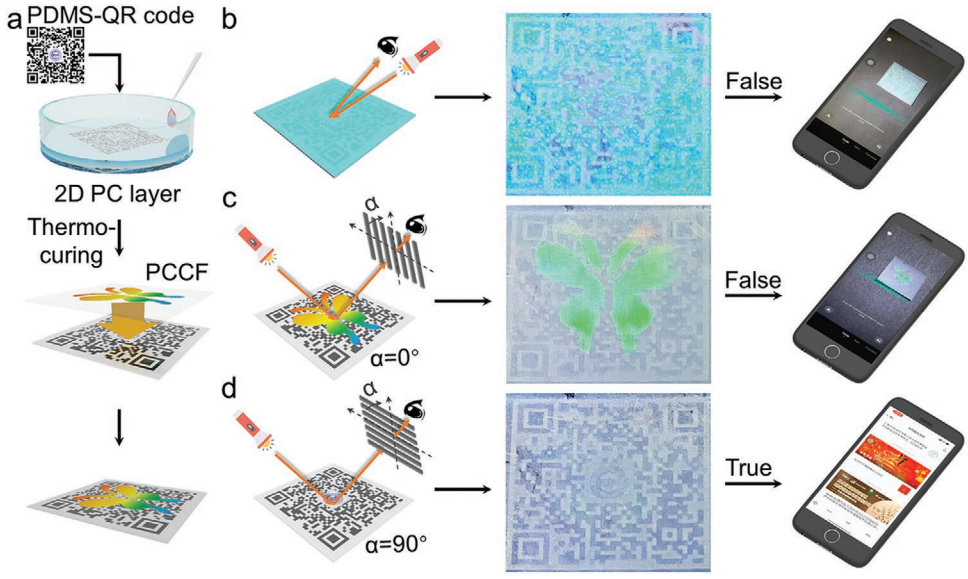

Figure 4. Schematic illustrations showing encryption and recognition of the paper-printed QR code encoded by PCCF. a) Schematic diagram of the preparation process of the paper-printed QR code encrypted by PCCF. b-d) The patterned PCCF displayed and hid the QR code (2.5 cm × 2.5 cm) under different viewing modes.

Information). Thus, the private information in the QR code can be almost perfectly protected by the PCCF, enabling information storage and exchange in a covert way. In addition, an information encryption label was constructed, as shown in Figure S11 (Supporting Information). The right information could be identified only through adjusting the viewing angle and the polarized angle to correct values simultaneously. Therefore, our proposed PCCF can also realize information encryption by two optical parameters that will increase the decryption difficulty and improve the encoding security.

To enhance the anti-counterfeiting level and expand practical applications in the information security field, we further create a "security label" that carries two distinct kinds of information by combining PCCF with 2D PC, which utilized the distinct different optical properties between PC and PCCF to realize the two-parameter controlled switchable images, as shown in **Figure 5**a. In this experiment, the Chinese character "牛" and a bull pattern were encoded into the PC structure and the PCCF structure, respectively, and then combined with a commemorative stamp (6 cm × 6 cm) to realize multiple anti-counterfeiting measures. Under white light, the anti-counterfeiting label demonstrates the colorful Chinese character "牛" and the bull pattern in the scattering state, as shown in Figure 5b. The structural color is angular-dependent, which is caused by the Bragg diffraction of the 2D PC, resulting in the distinct different color between the Chinese character "牛" and the bull pattern (Figure 5b, *Left*). Interestingly, we can "hide" the Chinese character "牛" by changing the viewing direction to the reflective angle to realize the image switching, which offers one dimension of anti-counterfeiting (Figure 5b, *Center*). In addition, both of the patterns could be "hidden" and the whole pattern of the stamp was revealed in the polarization state (Figure 5b, *Right*). These results demonstrate that the 2D PC layer and the PCCF layer contain independently encoded information and can enhance the confidentiality of information to meet the needs of specific situations.

3. Conclusion

We developed a simple and efficient surface patterning approach to construct a novel quasi-3D photonic architecture composed of an orderly closely packed monolayer PC and a regular micro-shallow pit structure. In these surface engineered PCCFs supported by self-assembling and nanoimprinting technique, strong angle-dependent structural color is generated from the regular 2D PC structure, while the high polarization property of structural color that is unachievable in traditional bilayer PC films is facilitated by the micro-shallow pit structure. This approach integrates the polarization effect and structural color onto the PCCF, which can be used for information encryption and anti-counterfeiting based on multidimensional control of the viewing angle and polarization. These properties of PCCF make it possible to realize multichannel image switching by using different optical parameters (i.e., scattering, diffraction, and polarization), which is a function seldom reported in previous works. Our approach, accompanied with great control of the degree of freedom by the optical parameters of incident light, opens new avenues for large-capacity and high-security 3D optical information encryption and anti-counterfeiting. Moreover, the random alignment between the two layers of PCCF (the closely packed monolayer of PS spheres and the periodic array of micro-shallow pits) can be employed as a unique fingerprint. Physical unclonable functions are based on random physical patterns generated by nature, which have a high complexity and unique nonreplicability to increase the level of information security. Thus, the PCCF provides a novel identification with full color, 3D

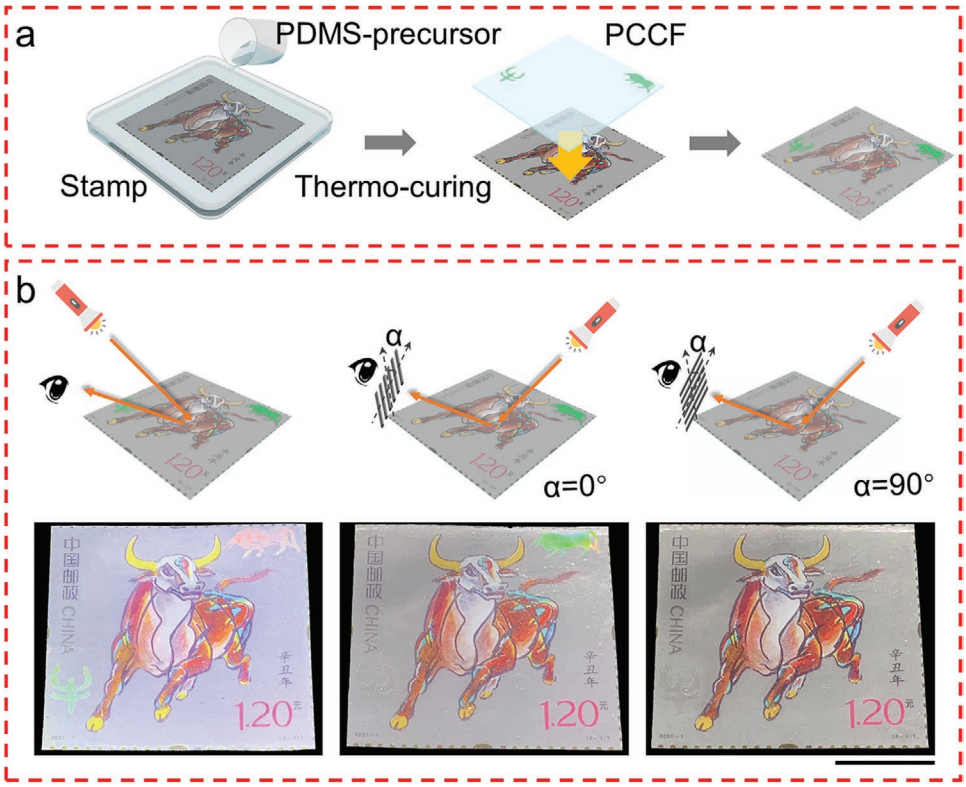

Figure 5. Demonstration of the PCCF-based material for real-time optical encryption and decryption. a) Schematic diagram of the preparation process of stamp encrypted by PCCF. b) Three-image switching under different viewing modes. Scale bar: 2 cm.

encryption, and fine nanostructure that is nearly impossible to replicate.

4. Experimental Section

All chemicals were used as received. These chemicals are Sylgard 184 polydimethylsiloxane (PDMS) (Dow Corning Corporation Ltd.); absolute ethanol (AR) (Beijing Chemical Works Corporation Ltd.); polystyrene (PS) microspheres (5 wt%, ≈600 nm in diameter) (Huge Biotechnology Corporation Ltd.); silicon dioxide (SiO_2) microspheres powders (≈2.5 µm in diameter) (Huge Biotechnology Corporation Ltd.); and sodium dodecyl sulfate (SDS). More details on the materials and methods can be found in the Supporting Information Appendix.

Supporting Information

Supporting Information is available from the Wiley Online Library or from the author.

Acknowledgements

This work was financially supported by the National Natural Science Foundation of China (22073107 and 21522308), National Key R&D Program of China (Grant No. 2018YFA0208500), Bureau of International Cooperation, Chinese Academy of Sciences (GJHZ201948), K.C. Wong Education Foundation, National Key R&D Program of China (Grant No. 2018YFA0208501), Projects External Cooperation Program of BIC, Chinese Academy of Sciences, Grant No. 121111KYSB20150022, and Youth Innovation Promotion Association CAS.

Conflict of Interest

The authors declare no conflict of interest.

Author Contributions

M.L. conceived the project and designed the experiments. X.L. carried out the experimental setup, fabrication, and measurements; X.L., Q.R., and F.V. worked on the simulations for the sample. X.L., Q.R., F.V., W.E.I.S., X.H., X.Y., Y.S., and M.L. wrote the text. X.L., Q.R., and F.V. contributed equally to this work.

Data Availability Statement

Research data are not shared.

Keywords

anti-counterfeiting, composite lattice photonic crystal, information multiplexing, polarization

Received: September 12, 2021
Revised: October 22, 2021
Published online:

[1] R. Arppe, T. J. Sørensen, *Nat. Rev. Chem.* **2017**, *1*, 0031.
[2] Z. Q. Li, X. Liu, G. N. Wang, B. Li, H. Z. Chen, H. R. Li, Y. L. Zhao, *Nat. Commun.* **2021**, *12*, 1363.

[3] Z. Zhao, H. Wang, L. R. Shang, Y. R. Yu, F. F. Fu, Y. J. Zhao, Z. Z. Gu, *Adv. Mater.* **2017**, *29*, 1704569.
[4] H. Z. Zheng, W. R. Li, W. Li, X. J. Wang, Z. Y. Tang, S. X. A. Zhang, Y. Xu, *Adv. Mater.* **2018**, *30*, 1705948.
[5] K. Zhong, J. Q. Li, L. W. Liu, S. V. Cleuvenbergen, K. Song, K. Clays, *Adv. Mater.* **2018**, *30*, 1707246.
[6] J. L. Liao, C. Zhu, B. B. Gao, Z. Zhao, X. J. Liu, L. Tian, Y. Zeng, X. L. Zhou, Z. Y. Xie, Z. Z. Gu, *Adv. Funct. Mater.* **2019**, *29*, 1902954.
[7] C. Li, M. X. Zhao, X. Zhou, H. Z. Li, Y. Wang, X. T. Hu, M. Z. Li, L. Shi, Y. L. Song, *Adv. Opt. Mater.* **2018**, *6*, 1800651.
[8] Q. T. Zhou, J. G. Park, J. Bae, D. Ha, J. Park, K. Song, T. Kim, *Adv. Mater.* **2020**, *32*, 2001467.
[9] G. Qu, W. Yang, Q. Song, Y. Liu, C. W. Qiu, J. Han, D. P. Tsai, S. M. Xiao, *Nat. Commun.* **2020**, *11*, 5484.
[10] Y. J. Bao, Y. Yu, H. F. Xu, Q. L. Lin, Y. Wang, J. T. Li, Z. K. Zhou, X. H. Wang, *Adv. Funct. Mater.* **2018**, *28*, 1805306.
[11] K. T. P. Lim, H. Liu, Y. Liu, J. K. W. Yang, *Nat. Commun.* **2019**, *10*, 25.
[12] Q. Wang, X. G. Zhang, H. W. Tian, W. X. Jiang, D. Bao, H. L. Jiang, Z. J. Luo, L. T. Wu, T. J. Cui, *Adv. Theory Simul.* **2019**, *2*, 1900141.
[13] L. Jin, Y. W. Huang, Z. Jin, R. C. Devlin, Z. Dong, S. Mei, M. Jiang, W. T. Chen, Z. Wei, H. Liu, J. Teng, A. Danner, X. Li, S. M. Xiao, S. Zhang, C. Yu, J. K. W. Yang, F. Capasso, C. W. Qiu, *Nat. Commun.* **2019**, *10*, 4789.
[14] S. Wang, Z. L. Deng, Y. J. Wang, Q. B. Zhou, X. l. Wang, Y. Y. Cao, B. Q. Guan, S. M. Xiao, X. P. Li, *Light: Sci. Appl.* **2021**, *10*, 24.
[15] X. Y. Fang, H. R. Ren, M. Gu, *Nat. Photonics* **2019**, *14*, 102.
[16] S. M. Xiao, V. P. Drachev, A. V. Kildishev, X. J. Ni, U. K. Chettiar, H. K. Yuan, V. M. Shalaev, *Nature* **2010**, *466*, 735.
[17] D. J. Hu, H. Li, Y. P. Zhu, Y. Q. Lei, J. Han, S. L. Xian, J. J. Zheng, B. O. Guan, Y. Y. Cao, L. Bi, X. P. Li, *Nat. Commun.* **2021**, *12*, 1154.
[18] S. N. Sheikholeslami, H. Alaeian, A. L. Koh, J. A. Dionne, *Nano Lett.* **2013**, *13*, 4137.
[19] J. X. Fan, L. Zhang, S. S. Wei, Z. Zhang, S. K. Choi, B. Song, Y. S. Sheng, *Mater. Today* **2021**, https://doi.org/10.1016/j.mattod.2021.04.019.
[20] J. C. Xue, Z. K. Zhou, L. M. Lin, C. Guo, S. Sun, D. Y. Lei, C. W. Qiu, X. H. Wang, *Light: Sci. Appl.* **2019**, *8*, 101.
[21] Y. L. Wang, H. Q. Cui, Q. L. Zhao, X. M. Du, *Matter* **2019**, *1*, 626.
[22] L. Qin, X. Liu, K. He, G. Yu, H. Yuan, M. Xu, F. Li, Y. Yu, *Nat. Commun.* **2021**, *12*, 699.
[23] R. L. Chen, D. C. Feng, G. J. Chen, X. D. Chen, W. Hong, *Adv. Funct. Mater.* **2021**, *31*, 2009916.
[24] Z. W. Li, Y. D. Yin, *Adv. Mater.* **2019**, *31*, 1807061.
[25] Z. L. Xie, X. Y. Zhang, H. L. Wang, C. Huang, H. D. Sun, M. Y. Dong, L. Ji, Z. F. An, T. Yu, W. Huang, *Nat. Commun.* **2021**, *12*, 3522.
[26] K. X. Li, C. Li, H. Z. Li, M. Z. Li, Y. L. Song, *iScience* **2021**, *24*, 102121.
[27] C. Li, X. Zhou, K. Wang, K. X. Li, M. Z. Li, Y. L. Song, *Compos. Commun.* **2019**, *12*, 47.
[28] J. Hou, H. C. Zhang, Q. Yang, M. Z. Li, Y. L. Song, L. Jiang, *Angew. Chem., Int. Ed. Engl.* **2014**, *53*, 5791.
[29] J. Hou, H. C. Zhang, B. Su, M. Z. Li, Q. Yang, L. Jiang, Y. L. Song, *Chem. Asian J.* **2016**, *11*, 2680.
[30] F. K. Bian, L. Y. Sun, L. J. Cai, Y. Wang, Y. J. Zhao, *Proc. Natl. Acad. Sci. USA* **2020**, *117*, 22736.
[31] Y. Qi, W. F. Niu, S. F. Zhang, S. L. Wu, L. Chu, W. Ma, B. T. Tang, *Adv. Funct. Mater.* **2019**, *29*, 1906799.
[32] Y. Qi, L. Chu, W. B. Niu, B. T. Tang, S. L. Wu, W. Ma, S. F. Zhang, *Adv. Funct. Mater.* **2019**, *29*, 1903743.
[33] S. Wu, T. Liu, B. Tang, L. Li, S. Zhang, *ACS Appl. Mater. Interfaces* **2019**, *11*, 10171.
[34] Y. Wang, W. Li, M. Li, S. Zhao, F. De Ferrari, M. Liscidini, F. G. Omenetto, *Adv. Mater.* **2019**, *31*, 1805312.
[35] M. Kolle, P. M. Salgard-Cunha, M. R. Scherer, F. Huang, P. Vukusic, S. Mahajan, J. J. Baumberg, U. Steiner, *Nat. Nanotechnol.* **2010**, *5*, 511.
[36] P. Vukusic, J. R. Sambles, C. R. Lawrence, *Nature* **2000**, *404*, 457.
[37] J. T. Zhang, L. Wang, D. N. Lamont, S. S. Velankar, S. A. Asher, *Angew. Chem., Int. Ed. Engl.* **2012**, *51*, 6117.
[38] K. X. Li, T. L. Zhang, H. Z. Li, M. Z. Li, Y. L. Song, *Acta. Phys -Chim. Sin.* **2020**, *35*, 1911057.
[39] C. Park, T. Lee, Y. Xia, T. J. Shin, J. Myoung, U. Jeong, *Adv. Mater.* **2014**, *26*, 4633.
[40] I. M. Krieger, F. M. O'Neill, *J. Am. Chem. Soc.* **1960**, *90*, 3114.
[41] L. Shi, H. W. Yin, X. L. Zhu, X. H. Liu, J. Zi, *Appl. Phys. Lett.* **2010**, *97*, 251111.
[42] A. E. Smith, C. D. Hause, *J. Opt. Soc. Am.* **1952**, *42*, 426.
[43] D. H. Goldstein, *Polarized light*, 2nd ed., Marcel Dekker, New York **2003**.
[44] R. P. O'Shea, G. P. Misson, S. E. Temple, *Curr. Biol.* **2021**, *31*, R178.